

SCIENTIFIC REPORTS



OPEN

Joining Chemical Pressure and Epitaxial Strain to Yield Y-doped BiFeO₃ Thin Films with High Dielectric Response

Received: 04 February 2016

Accepted: 19 April 2016

Published: 09 May 2016

N. D. Scarisoreanu¹, F. Craciun², R. Birjega¹, V. Ion^{1,3}, V. S. Teodorescu⁴, C. Ghica⁴, R. Negrea⁴ & M. Dinescu¹

BiFeO₃ is one of the most promising multiferroic materials but undergoes two major drawbacks: low dielectric susceptibility and high dielectric loss. Here we report high in-plane dielectric permittivity ($\epsilon' \sim 2500$) and low dielectric loss ($\tan \delta < 0.01$) obtained on Bi_{0.95}Y_{0.05}FeO₃ films epitaxially grown on SrTiO₃ (001) by pulsed laser deposition. High resolution transmission electron microscopy and geometric phase analysis evidenced nanostripe domains with alternating compressive/tensile strain and slight lattice rotations. Nanoscale mixed phase/domain ensembles are commonly found in different complex materials with giant dielectric/electromechanical (ferroelectric/ relaxors) or magnetoresistance (manganites) response. Our work brings insight into the joined role of chemical pressure and epitaxial strain on the appearance of nanoscale stripe structure which creates conditions for easy reorientation and high dielectric response, and could be of more general relevance for the field of materials science where engineered materials with huge response to external stimuli are a highly priced target.

Multiferroics (MF) are materials which have simultaneously more ferroic properties, such as ferroelectric, antiferrodistortive or magnetic order¹. The multitude of their properties is given by the coupling between the various ferroic orders, which can boost the developing of new multifunctional devices.

Among MF, BiFeO₃ (BFO) is certainly the most investigated due to both polar and magnetic orders coexisting at room temperature, which are of interest for potential applications in nonvolatile memories, spintronics, piezoelectric devices etc². The interplay between its ferroic order parameter and the various structural degrees of freedom gives rise to a complex phase diagram². Thus, below the critical temperature $T_c \approx 1100$ K, BFO transforms from the paraelectric orthorhombic (O) Pnma phase into the rhombohedral (R) R3c ferroelectric (FE) phase. The rhombohedral R3c ground state is characterized by antiphase octahedral tilts about the [111]_c directions and ionic displacements from the centrosymmetric positions along the same axis, with pseudocubic lattice parameters $a = 3.965$ Å and $\alpha = 89.4^\circ$ ³. Below the Néel temperature $T_N \sim 640$ K BFO has also a G-type antiferromagnetic (AFM) ordering of Fe³⁺ ions⁴.

Among the drawbacks of BFO, the small dielectric constant, high dielectric loss and high leakage currents, which are detrimental for its applications in electromechanical devices, must be pointed out. The intrinsic dielectric constant at radio frequencies was measured to be about 30⁵. At lower frequencies (kHz and MHz range) higher values (up to a few hundreds²) have been measured, however they decrease with frequency and are accompanied by high dielectric losses, which are the fingerprint of space charge contributions². The small intrinsic dielectric value has been attributed to the far away critical temperature T_c^2 .

There are two main ways to control the phase stability and transition temperatures in BFO: one is through strain engineering and the other is through chemical substitutions. Both aim to induce, by different means (mechanical pressure or chemical pressure) a mixed state, characterized by coexisting phases, in order to improve its dielectric and electromechanical response. The two degrees of freedom, polar displacements and oxygen

¹National Institute for Laser, Plasma and Radiation Physics, 077125 Magurele, Romania. ²CNR-ISC, Istituto dei Sistemi Complessi, Area della Ricerca di Roma-Tor Vergata, Via del Fosso del Cavaliere 100, I-00133 Rome, Italy.

³Faculty of Physics, University of Bucharest, 077125 Magurele, Romania. ⁴National Institute of Material Physics, 077125, Magurele, Romania. Correspondence and requests for materials should be addressed to N.D.S. (email: nicu.scarisoreanu@inflpr.ro)

octahedral tilts which coexist in a wide temperature range, can react differently to chemical substitutions or external parameter variations and thus lead to a multitude of phases. Thus BFO is very sensitive to the application of an external pressure: above 10 GPa the pressure brings the high temperature phase (O Pnma) at room temperature while, at lower pressures, several low symmetry (monoclinic) phases are stabilized at room temperature⁶. This is important, taking into account that the stress established within the plane of growth in epitaxial films can reach several GPa⁷. The strain can be exerted in a controlled manner in thin films and the strain engineering is currently used to tune their functional properties⁸. In thin film form the crystallographic structure of epitaxial thin films often deviates from the bulk due to strain. For instance BFO films grown on low misfit substrates adopt a monoclinic (M) structure for compressive strain^{9,10}. Thus BFO epitaxial films with thicknesses in the range 40–960 nm grown on SrTiO₃ (STO) (001) substrates¹¹ change from angularly distorted tetragonal-like to monoclinic and finally to more bulk-like distorted rhombohedral structures as the strain relaxes with increasing thickness. Similar results have been reported by Saito *et al.*¹² for BFO films grown on STO (001) substrates with thicknesses varying in the range 15–500 nm. Thus for films with thickness below 50 nm a fully strained structure with tetragonal symmetry was obtained, while for more relaxed films (with thickness above 50 nm) a monoclinic structure with continuously varying lattice parameters was observed. Remarkably, a rhombohedral bulk-like structure was not found even for the thickest films. Similar results have been reported by Kan and Takeuchi¹³. BFO films with thicknesses 50 nm–1000 nm grown on STO (001) showed monoclinic symmetry with different lattice parameters, depending on film thickness, thus on the degree of strain relaxation.

As previously stated, an alternative way to tune materials at the boundary between different but energetically equivalent structural phases is through chemical substitutions. As a consequence, huge response at weak external signals can be obtained in the presence of an energy landscape of multiple phases close in energy¹⁴.

Recent research on doped BFO focused on structural and electromechanical properties of rare earth (RE) substituted BFO thin films^{15,16}. A strong dependence on the ionic radius of the substituted elements has been observed. When rationalized in terms of the average A-site radius, a R-O structural transition was observed at the same average radius value, independently of the RE ion type. Based on results obtained on doping with different concentrations of RE ions, a universal phase diagram in terms of ionic radius has been proposed^{17,18}.

The size of RE ions controls also the stability of the structural phase, as shown by the temperature dependence of the lattice parameters¹⁷. Thus, a stronger chemical pressure, induced by the smaller ionic radius of the substituting RE elements extends the orthorhombic phase towards lower composition and temperature range. Transmission electron microscopy (TEM) on RE-BFO substituted films evidenced the presence of different competing phases in a narrow composition range associated with a morphotropic phase boundary (MPB). The MPB is related to a structural transition from the FE R phase to an O phase, with enhancement in the dielectric constant and piezoelectric coefficient. For example in Bi_{1-x}Sm_xFeO₃ films grown on STO (001) substrates the MPB around room temperature was found for compositions with $x \cong 0.14$ ¹⁶. For smaller radius RE dopants (RE = Gd³⁺, Dy³⁺) the MPB occurred at smaller x values (0.12 for Gd and 0.07 for Dy). In all Bi_{1-x}RE_xFeO₃ compositions it was found that the transformation from the R phase to the O phase at MPB is associated with a nanoscale phase mixture composed of the parent BFO R lattice and lamellar ferroelectric nanodomains with alternating polarizations^{16,19}. Thus the occurrence of such complex phase coexistence was considered responsible for the enhanced dielectric and piezoelectric response at MPB, by providing a low energy pathway for the polarization transition between the different polar axes. Indeed an enhanced dielectric constant (~ 300) was measured for MPB Bi_{1-x}RE_xFeO₃ (RE = Sm, Gd, Dy) compositions at room temperature¹⁷. These results have been obtained on films with 200 nm thickness entirely relaxed, thus the epitaxial strain was playing no role in their properties¹⁷.

We take further this investigation and address the problem of concomitant influence of RE-doping and epitaxial strain on BFO properties. For doping, a RE ion (Y³⁺) with smaller ionic radius has been chosen. We show that Y-BFO films with thickness about 100 nm display very high in-plane dielectric constant. We relate this huge enhancement to the destabilizing influence of the chemical pressure induced by the small size ion substitution and the peculiar nanostripe formation due to partial strain relaxation. Our results can be of more general relevance for other materials where properties improvement is pursued through the combined role of chemical pressure (doping) and epitaxial strain.

Results and Discussion

We have employed pulsed laser deposition (PLD) technique to grow Bi_{1-x}Y_xFeO₃ (Y-BFO) epitaxial thin films with thickness of about 100 nm on STO (001) single crystal substrates. For comparison, pure BiFeO₃ (BFO) thin films have been grown also, on the same type of substrates. As further described in the Experimental section, a relatively low growth rate (~ 0.1 Å/s) and high deposition temperature (~ 700 °C) have been selected for deposition. The deposition conditions have a strong influence on the final lattice parameters and tetragonality of the BFO films. Indeed it has been shown that tetragonal-like BFO films can be grown even on low-mismatch substrates such as STO by controlling the growth rate and deposition temperature^{20–23}. Namely, at low growth rates and/or high substrate temperature the incident adatoms can diffuse more easily and follow the substrate lattice, while at high growth rates or low deposition temperature the arriving adatoms will accumulate in island-type zones where a high strain state is created. These high strain areas favour the tetragonal symmetry of the films, with high tetragonality ratio²¹. However, we have preferred to work with a low growth rate and high deposition temperature in order to promote a layer-by-layer-like growth and smooth surface.

The selected composition was Bi_{0.95}Y_{0.05}FeO₃. Figure 1(a) shows a schematic view of the tilt distortions ($a'a'a'$ system in Glazer's notation²⁴) in the ground R3c structure of a RE-doped BFO, where the black spheres in the interstices between oxygen octahedra represent Bi ions, while the smaller (orange) sphere is the RE ion.

It is clear that the smaller its radius is the larger is the available space for the tilting of oxygen octahedra in the structure and easier is the appearance of a new structural phase. Figure 1(b) shows the lattice constants of our Y-BFO films, placed in the context of a typical variation of BFO lattice constants with film thickness, as reported

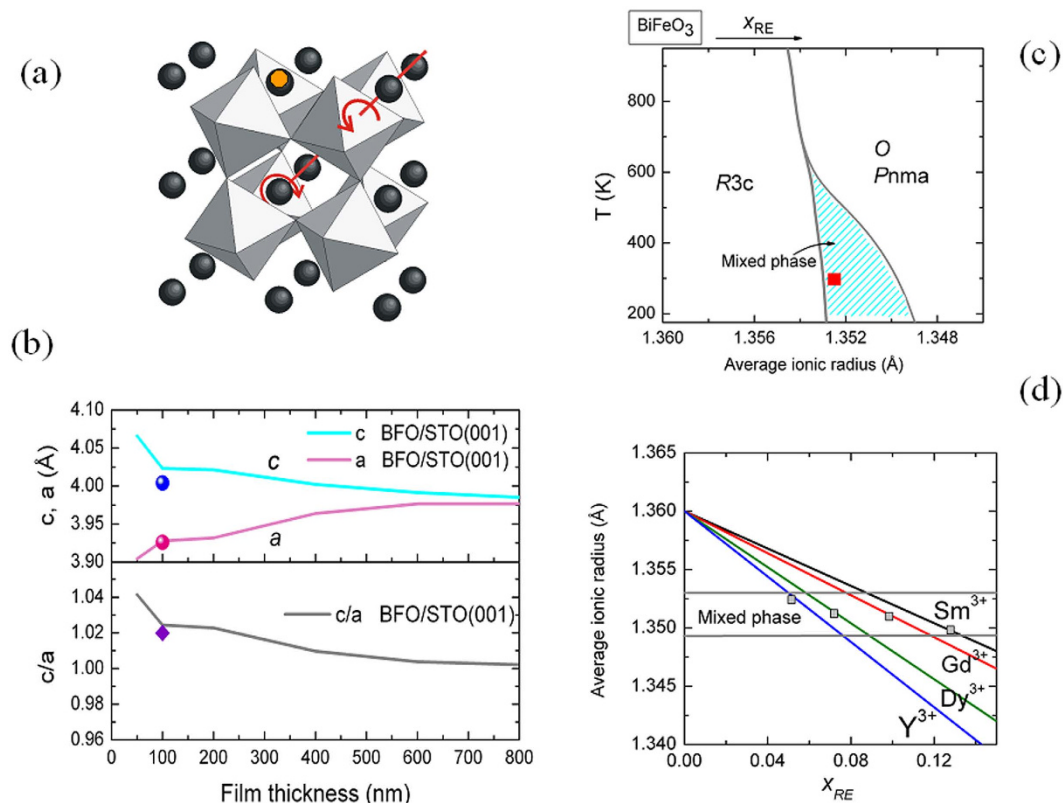


Figure 1. (a) Schematic view of the tilt distortions in the ground R3c structure of a RE-doped BFO, where the black spheres in the interstices between oxygen octahedra represent Bi³⁺ ions, while the smaller (orange) sphere is the RE ion; (b) Lattice constants and tetragonality ratio of Y-BFO films, represented by points. For comparison, the curves of variation of the BFO parameters with film thickness, as reported in ref. 13, are also shown; (c) A schematic of the universal phase diagram of RE-doped BFO, as reported in refs 16,17. The red square represents the selected composition for our films, in terms of average ionic radius; (d) Average ionic radius - *x* dependence, for different RE elements, calculated as described in the text.

in ref. 13. Figure 1(c,d) shows our selected composition Bi_{0.95}Y_{0.05}FeO₃ in the context of temperature - average ionic radius¹⁷ and average ionic radius - RE concentration diagrams. There will be more comments on these figures in the further discussion. In order to compare the properties of Y-BFO films with those of the undoped BFO films, another set of samples deposited on STO in the same conditions starting from pure BFO targets has been examined.

Figures 2(a) and 3(a) show the θ -2 θ X-ray diffraction patterns of the Y-BFO (film 1) and BFO films. A detail around the (002) reflection is shown in Fig. 2(b). Only (00l) reflections of Y-BFO and BFO films and STO substrate are observed, demonstrating the pure phase and epitaxial growth of the films. In-plane and out-of-plane lattice parameters were determined from single scans through the symmetric (00l) and asymmetric (hkl) reflections, respectively. The structural parameters of the films (in pseudocubic notation) are listed in Table 1. The out-of-plane lattice parameter *c* has been found to be 4.0042 Å for Y-BFO film, slightly larger in comparison with the BFO film (3.9983 Å). We recall that for Bi_{0.95}Y_{0.05}FeO₃ ceramics the pseudocubic lattice parameter is about 3.94 Å²⁵. Thus the out-of-plane lattice parameter *c* of the Y-BFO films exceeds the bulk pseudocubic lattice parameter, while the in-plane lattice parameter *a* is about 3.9266 Å, fairly close to the cubic STO substrate lattice parameter (3.905 Å). The tetragonality ratio *c/a* has been found to be about 1.02, slightly larger in comparison with the value obtained for the BFO film. The difference between the out-of-plane and in-plane lattice constants is attributed to compressive coherent in-plane strain induced by the STO substrate which causes a cell elongation in the out-of-plane direction. In Fig. 1(b) we have compared this pseudo-tetragonal distortion with results previously reported in literature for BFO films grown by pulsed laser deposition¹³. For a film thickness of about 100 nm the lattice distortion is similar and the films are in a partially relaxed strain state. From our results we cannot say more about the cell symmetry, but there is by now a general consensus that BFO films grown on STO (001) substrates show monoclinic symmetry for a wide range of film thicknesses^{13,26–28}.

The degree of in-plane orientation was assessed by the XRD Φ -scans. As shown in Figs 2(c) and 3(b) the peaks of the (101) reflection of the Y-BFO and BFO films occur at the same azimuthal Φ angles as those for STO (101) substrate reflection and are 90° apart from each other. This indicates the presence of fourfold symmetry with a “cube-on-cube” epitaxial growth on the STO (001) substrate.

The full width at half maximum (FWHM) values of the rocking curve of the (002) Y-BFO diffraction peak is larger in comparison with the (002) diffraction peak of the pure BFO film due to both the monoclinic distortion

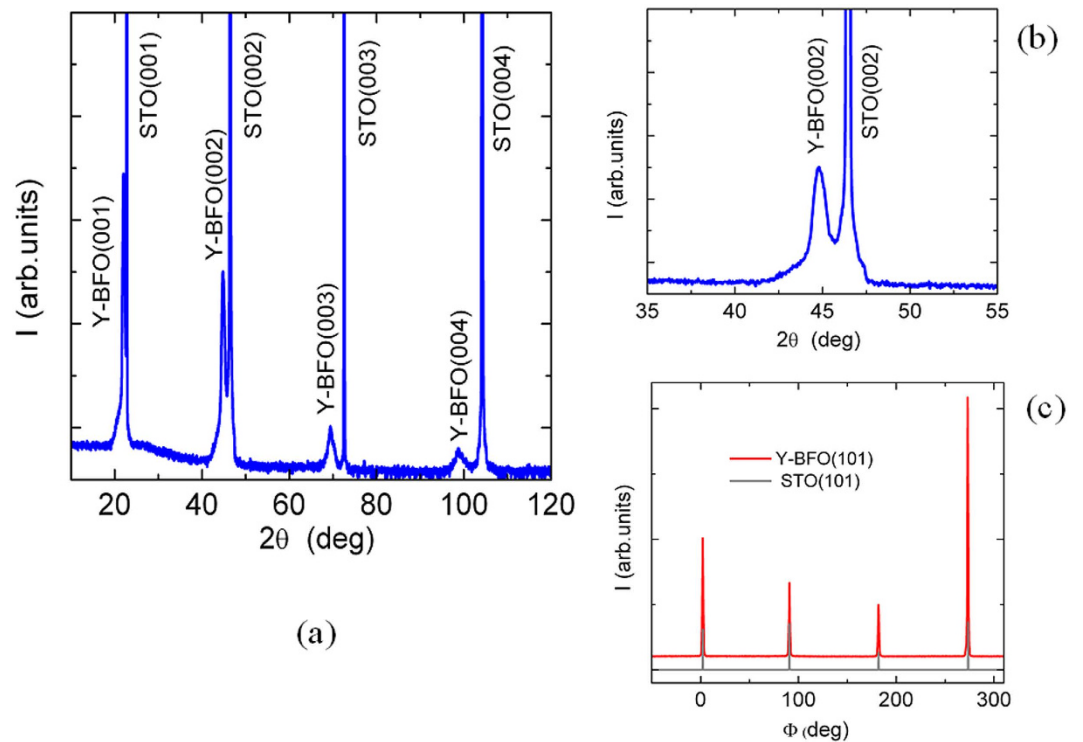


Figure 2. (a) The θ - 2θ diffraction patterns of the Y-BFO films; (b) A detail around the (002) reflection; (c) XRD Φ -scans showing the (101) reflections of the Y-BFO film and STO substrate.

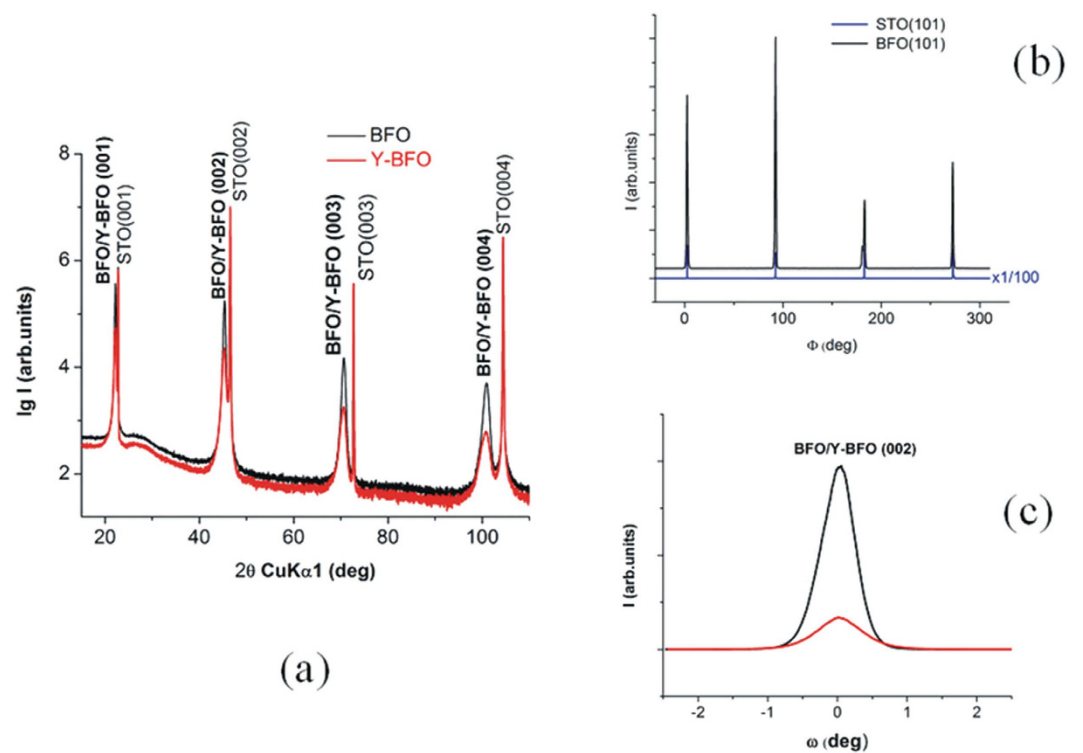


Figure 3. (a) Comparison between θ - 2θ diffraction patterns of the Y-BFO and BFO films; (b) Comparison between Φ -scans for the same samples; (c) Full width at half maximum (FWHM) values of the rocking curve of the (002) diffraction peaks for Y-BFO and BFO films.

Sample	<i>c</i> (Å)	<i>a</i> (Å)	<i>c/a</i>	Microstrain ε_{\perp} (%)	RK(200) ω -scan (deg)	L_{\parallel} (nm)	α_{tilt} (deg)
Y-BFO	4.0042	3.9263	1.0198	0.322	0.7829	70	0.8615
BFO	3.9983	3.9600	1.0097	0.199	0.5895	239	0.5195

Table 1. Structural data extracted from XRD analysis.

in the out-of-plane direction and dopant-induced lattice modifications (Fig. 3c). Similar analysis performed on a second set of Y-BFO films (film 2) grown in the same conditions yield comparable results (see the Supplementary Information). The Supplementary Information includes XRD patterns of the high angle peak (004) of the Y-BFO (film 2) in comparison with the Y-BFO (film 1) and the reference BFO film, as well as the superimposed rocking curves of the (002) peaks.

The substitution with Y on the B-site apparently causes a decrease of the in-plane lattice parameter and an increase of *c/a* ratio with respect to BFO film lattice (Table 1). In order to better understand the effect of the Y-dopant on the films, an Williamson-Hall approach was used to separate the various possible contributions to the broadening of XRD reflections²⁹. The method is based on the assumption that an epitaxial film consists of single crystallites, defect-free domains, named mosaic blocks, with a mean vertical and lateral dimension called vertical and lateral coherence length^{29,30}. The terms lateral and vertical are associated to directions parallel and perpendicular to the substrate surface, respectively. The vertical coherence length is to be connected to films thickness for systems with defects running mainly parallel to the substrate surface normal. The mosaic blocks are assumed to be slightly misoriented with respect to each other, the out-of-plane rotation of the blocks being called mean mosaic tilt angle^{29,30}. The vertical coherence length, L_{\perp} and the heterogeneous microstrain Bragg reflection ε_{\perp} are derived from the Williamson-Hall plots²⁹ using the radial scan (ω -2 θ scan) directions of (00*l*) symmetric reflections, by using the following relation

$$\frac{\beta \cos \theta}{\lambda} = \frac{1}{L_{\perp}} + 4\varepsilon_{\perp} \frac{\sin \theta}{\lambda} \quad (1)$$

where λ is the X-ray wavelength, β - the integral breadth (instrumental corrected FWHM) and θ - the Bragg angle. The plot of $(\beta \cos \theta)/\lambda$ versus $(\sin \theta)/\lambda$ gives the value of the strain from the slope and the vertical coherence length from the ordinate intercept.

From the broadening of the rocking curve (ω scan) of the same symmetric (00*l*) reflections, using a similar Williamson-Hall approach proposed by Mentzger *et al.*³¹, the coherence length parallel to the substrate surface L_{\parallel} and the tilt angle α_{tilt} could be extracted. All the XRD results are summarized in Table 1, revealing the effect of Y-doping. The Y-BFO films exhibit the following features in comparison with the undoped BFO film: higher microstrain values, slightly larger tilt angles and an important decrease of their lateral coherence lengths. This last aspect is to be related with the formation of smaller nanodomains parallel to the substrate.

Figure 4 shows a cross-sectional HRTEM image of the Y-BFO film and the corresponding fast Fourier transform (FFT) pattern (Fig. 4a) used for the strain analysis. The HRTEM image evidences contrast variation across nanodomain stripes with widths of 5–20 nm, oriented approximately along the x-x direction (Fig. 4b), which has been selected along the 001 direction of the Y-BFO structure (parallel to the substrate normal). The FFT pattern of this region shows the fundamental perovskite reflections with spot splitting or diffused elongation due to the tilted stripe nanodomain structure.

A microstrain analysis has been performed on the HRTEM image by geometric phase analysis (GPA)³². The variation of strain has been analysed along two directions Ox and Oy oriented perpendicular (ε_{xx} in Fig. 4c) and parallel (ε_{yy} in Fig. 4d) to the substrate normal. Line profiles of ε_{xx} and ε_{yy} strains obtained on the marked zones are displayed in Fig. 4(e,f), respectively. In the strain maps the blue zones are under strong compressive strain, the red ones are under strong tensile strain while the green ones are not strained. Small ε_{xx} strain variations are observed along the stripes, alternating sign with an average “period” of a few nm. However the most interesting strain variation is found on the perpendicular direction, where an alternation of compressive and tensile ε_{yy} strains is registered across the stripes. A detailed analysis in different zones evidences small lattice rotations between different stripes. This shows that both lattice cell as well as stripe orientation variations, compatible with monoclinic distortion, occur in strained Y-BFO films.

Comparative HRTEM and stress/strain GPA maps of the Y-BFO and BFO films are shown in Fig. 5 (a–d). These analysis evidenced that the pure BFO films do not show stripe modulation, as confirmed by the uniform aspect of the HRTEM image (Fig. 5b), but they are still strained due to the substrate influence. The major difference is that the strain level in BFO film is lower and almost uniformly distributed (Fig. 5d). The line profile shown in Fig. 5(f) evidences that the strain variations are much smaller than in Y-BFO film (Fig. 5e), therefore we can presume that nanostripe formation occurs only for Y-BFO films. These assertions are supported also by the structural data extracted from XRD analysis (Table 1), which show that BFO thin films are characterized by lower microstrain and larger lateral coherence length values than Y-BFO films.

There are multiple evidences that, in partially relaxed films, the in-plane strain does not relax to zero but locally oscillates, by different mechanisms, including monoclinic twinning rotation³³. Moreover, for the case when the epitaxial constraint is partially relaxed, it has been observed that the result is a nanoscale mixed-phase structure³⁴, with the lattice mismatch accommodated by the gradual deformation of the structure between different phases. This nanoscale mixed-phase ensemble has been compared to the relaxor ferroelectrics and to the colossal magnetoresistance (CMR) manganites, which show similar features, and where a relatively low signal can activate a large response³⁴.

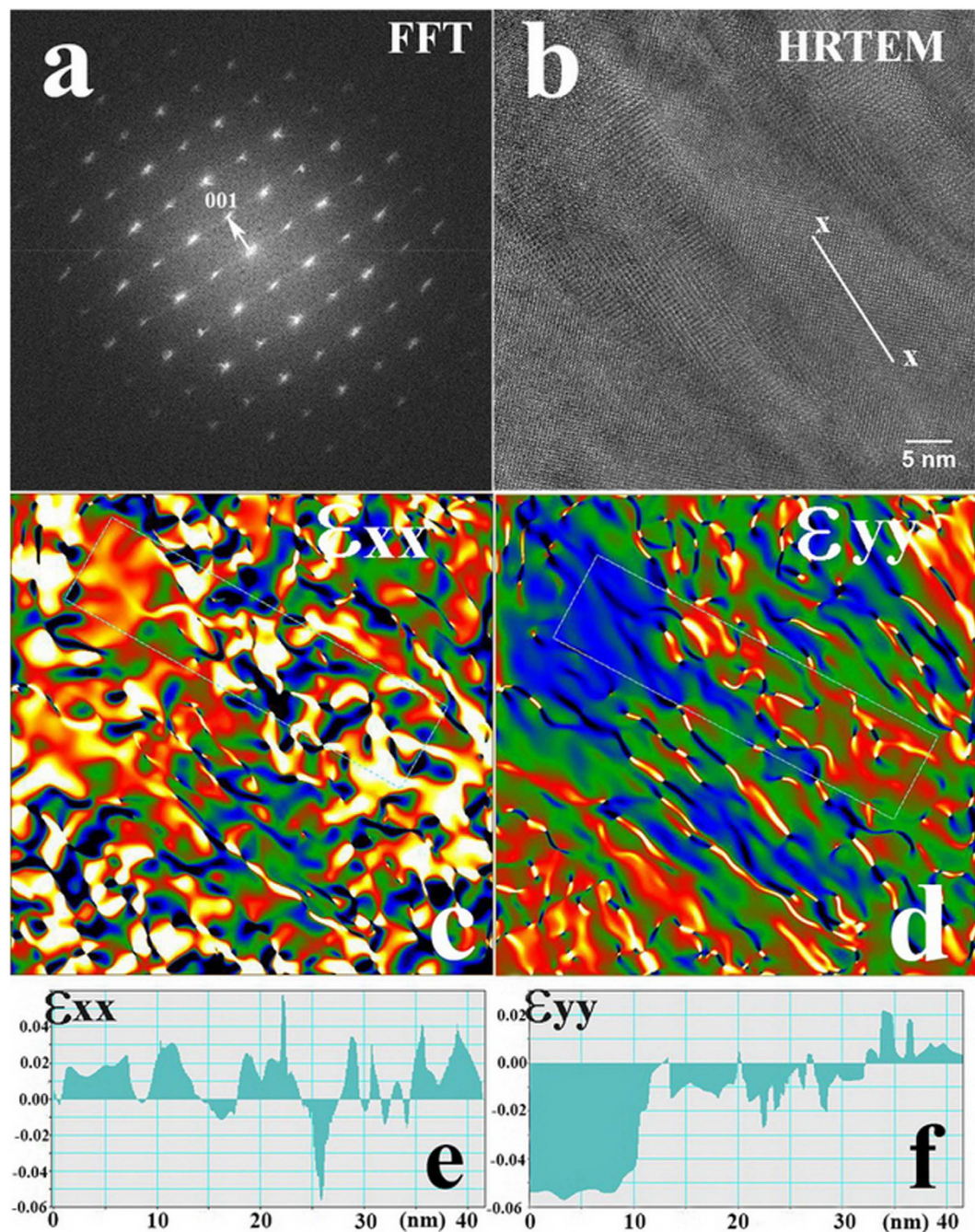


Figure 4. (a) Fast Fourier transform (FFT) pattern used for the strain analysis corresponding to the cross-sectional HRTEM image of the middle zone of the Y-BFO film shown in (b). (c) Microstrain analysis performed on the HRTEM image by geometric phase analysis (GPA) along the Ox direction; (d) the same for the Oy direction; (e), (f) Line profiles of ϵ_{xx} and ϵ_{yy} strains, respectively, obtained on the marked zones displayed in the previous images.

The additional distortions associated with the presence of nanodomains are related to the elastic bending and rotation of the lattice planes in order to fit the adjacent domains. They result into nanostructures with contrast difference as seen in Fig. 6(a). These nanostructures have widths of about 10 nm and an additional detailed GPA analysis has been performed in order to evidence their rotation. Thus Fig. 6 displays lattice rotation analysis on the Y-BFO film, operated on a representative HRTEM image taken on the middle region of the film, shown in Fig. 6(a), together with the power spectrum corresponding to this image area (Fig. 6b) and the phase image corresponding to the same area, calculated for the (110) reflexion in the power spectrum (Fig. 6c). The local lattice rotation was calculated using GPA³². The resulting lattice rotation along the rectangular area indicated in the phase image, connecting the green and the red areas, is displayed in Fig. 6(d). It can be observed that the Y-BFO lattice in the

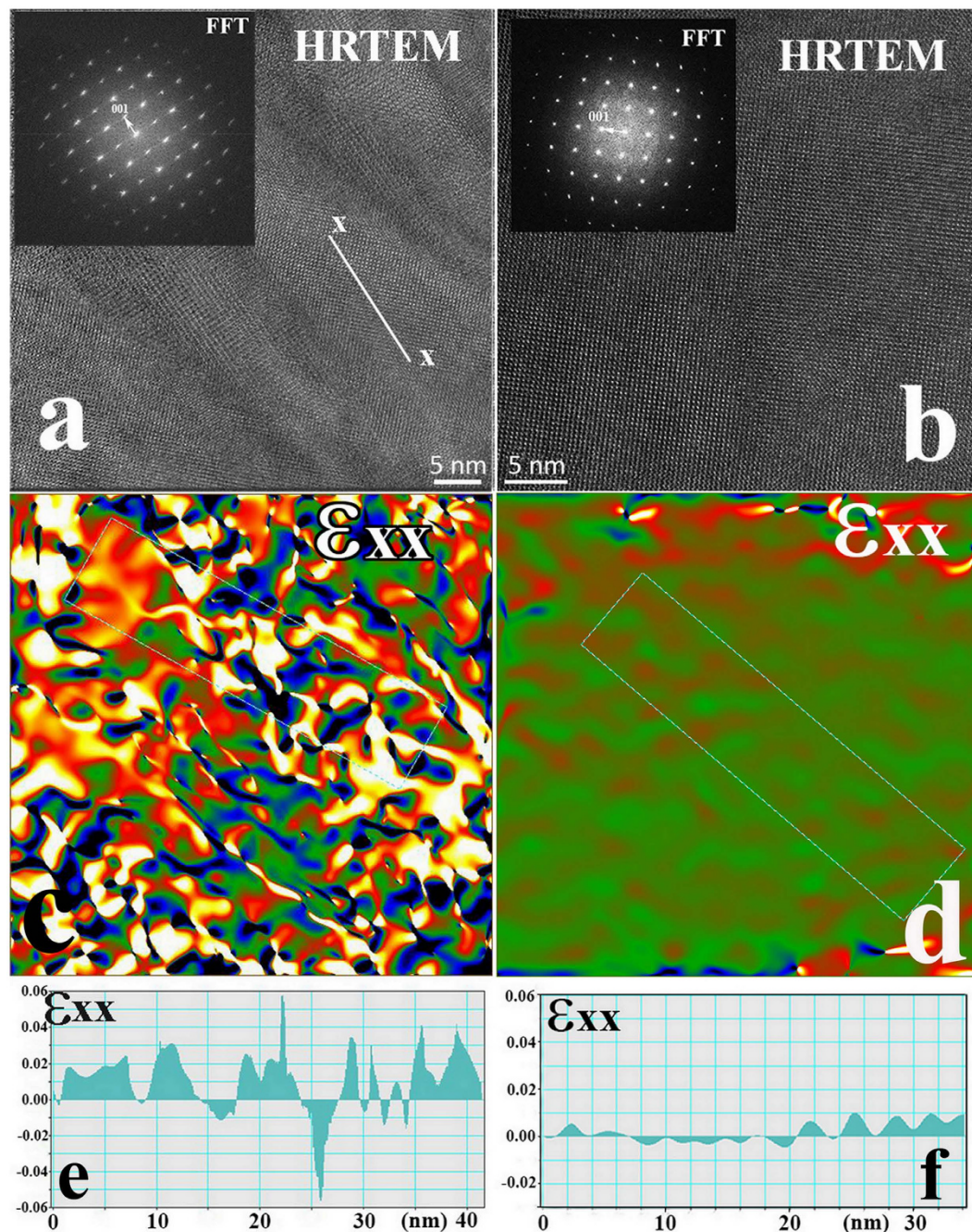


Figure 5. Comparative HRTEM, FFT and stress/strain GPA maps and line profiles of the Y-BFO (a,c,e) and BFO (b,d,f) films far from the interface.

green area is rotated by about 1.5 degrees in the positive sense while the red area is rotated by about 2 degrees in the negative sense. The total rotation between the green and the red domains is about 3.5 degrees.

In Fig. 7(a) a piezoforce microscopy (PFM) phase image measured on a Y-BFO film surface is shown, together with a typical line profile (Fig. 7b). The out-of-plane PFM response shows strong domain contrast, indicating that the material is polar with a polarization vector oriented mainly along the *c*-axis. Domains are identified as being polarized either into the specimen surface or out of the sample, depending on dark or light normal PFM phase contrast, respectively. The line profile shows that the phase difference between the zones with different contrast is nearly 180°.

Dielectric spectroscopy measurements have been made on interdigital electrodes (IDE) deposited on top surfaces of the films (10 IDE structures on each sample). A sketch of the IDE structure is shown in the inset in Fig. 8. The measurements yield the capacitance and the dielectric loss $\tan \delta$. Each IDE consists in $N = 21$ finger pairs of length $L = 464 \mu\text{m}$ and width $10 \mu\text{m}$. The interspace between fingers is $10 \mu\text{m}$, thus the distance D between finger centres is $20 \mu\text{m}$. A second set of similar samples but provided with IDE of different dimensions ($N = 15$, $L = 1200$

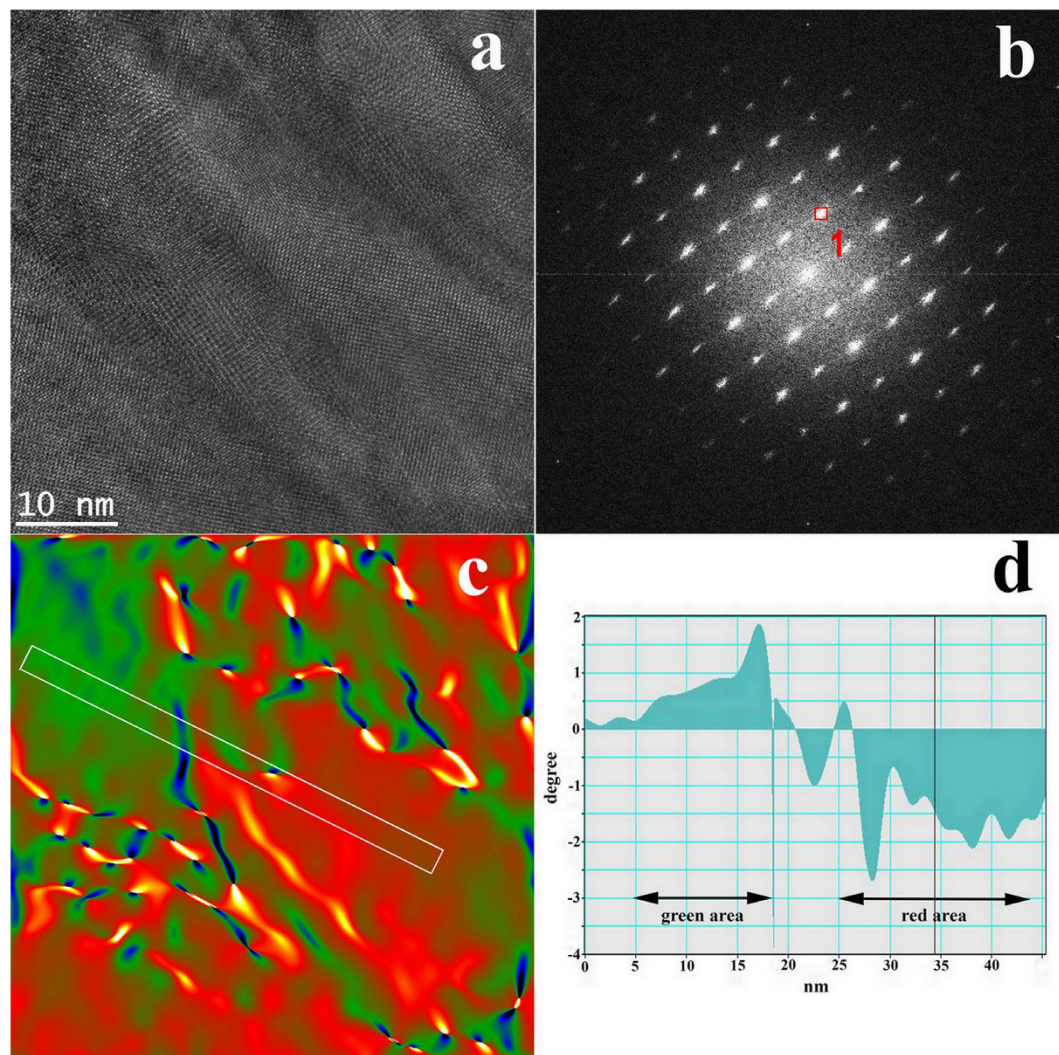


Figure 6. (a) HRTEM image of the Y-BFO film, taken on the middle region of the film; (b) Power spectrum corresponding to this image area; (c) GPA analysis performed on the same area in order to evidence local lattice rotations; (d) Resulting local lattice rotation along the rectangular area indicated in the phase image.

μm , width = 7.5 μm , $D = 15 \mu\text{m}$) has been prepared and investigated, in order to rule out the possible influence of IDE characteristics on the measured values.

The in-plane dielectric constant of the Y-BFO thin film capacitors with the interdigital electrode configuration was calculated by using the analytical model derived by Farnell *et al.*³⁵ and further developed in ref. 36. It has been shown that the dielectric constant of the thin film ϵ can be calculated using the Eq. (2)

$$\epsilon = \epsilon_S + \frac{C_n - C_K(1 + \epsilon_S)}{C_K(1 - \exp(-4.6h/D))} \quad (2)$$

where ϵ_S is the dielectric constant of the substrate, h is the film thickness ($h = 100 \text{ nm}$), C_K is a constant depending on IDE geometry and C_n is the measured capacitance of the IDE normalized to the finger length (L) and to the number of fingers ($2N - 1$). In the case of IDE patterns with equal finger width and spacing the constant $C_K = 4.53 \text{ pF/m}^{35,36}$. The dielectric constant of the STO substrate is ~ 300 .

The Y-BFO dielectric constant and loss values measured on 6 representatives IDE are plotted in Fig. 8. The values measured at 10 kHz are about 2500 (on one transducer a value > 3000 was obtained). The dielectric loss is very small (~ 0.007). Moreover, neither the losses nor the dielectric constant show significant variation in the frequency range 1 kHz–1 MHz.

The values obtained for the dielectric constant are by far the highest obtained for BFO, bulk or thin film, pure or doped. In order to verify the experimental procedure and the calculation method, measurements have been repeated on IDE electrodes directly deposited on the substrate and the same model has been applied to calculate the dielectric constant. Perfect agreement has been obtained between the measured and the data sheet value of the STO dielectric constant.

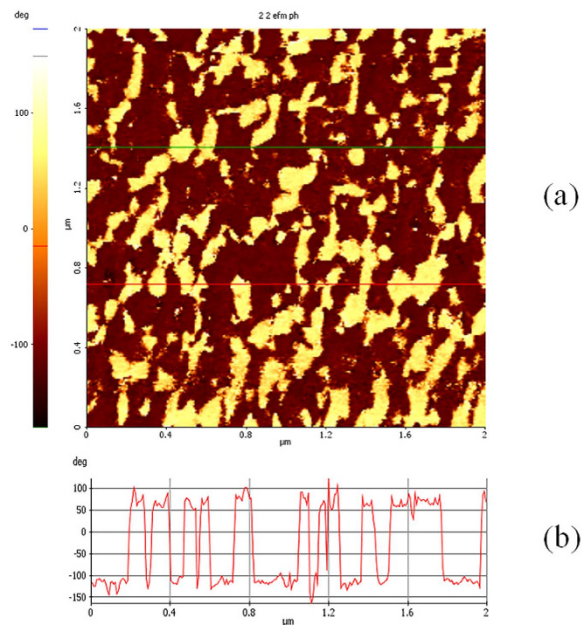


Figure 7. (a) Out-of-plane PFM phase image measured on a Y-BFO film surface. The domains are polarized into the specimen surface or out of the sample, as indicated by the dark or light normal PFM phase contrast, respectively; (b) The line profile shows that the phase difference is nearly 180° .

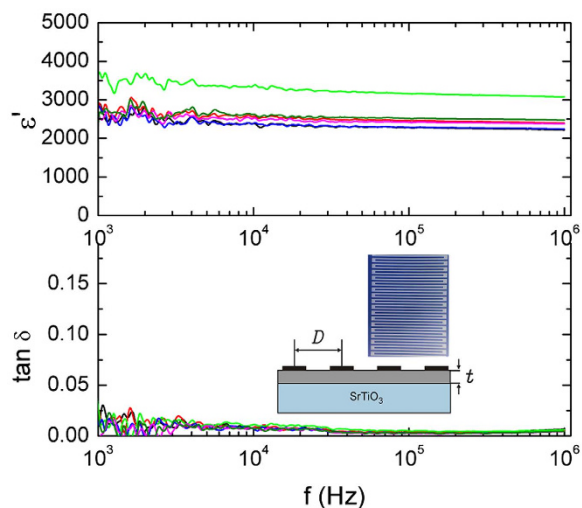


Figure 8. Y-BFO dielectric constant and loss tangent values, measured on 6 representative IDE in the frequency range 1 kHz-1 MHz. A sketch of the IDE structure is shown in the inset.

Dielectric measurements have been made on a second set of Y-BFO films with IDE electrodes with different dimensions and number of fingers and the results are similar which rule out possible effects of geometric configuration on the measurements (see Supplementary Information). For comparison we have also investigated the dielectric properties of pure BFO films on which similar IDE electrodes have been deposited. Typical results (as obtained on many IDE electrodes) are shown in Fig. 9, as well as in the Supplementary Information. Although the dielectric constant shows a high value, it is however much smaller than for Y-BFO films.

We have analyzed above the effects of strain on the Y-BFO films, which manifest by the appearance of a stripe nanodomain structure with monoclinic symmetry. Stripe-like domain patterns have been identified also in other ferroelectric³⁷ or relaxor-ferroelectric systems³⁸ and in BFO films grown on different substrates^{39,40}.

We believe that this peculiar nanostructure could be at the origin of the observed huge dielectric response. However we need to analyze also the influence of small radius Y^{3+} ions on the microstructure and dielectric response of Y-BFO films, by taking advantage of the reported findings on the universal phase diagram of RE-substituted BFO¹⁷. In Fig. 1(c) the plot lines represent schematically the phase diagram temperature (T)-average ionic radius (R_{av}) of $Bi_{1-x}RE_xFeO_3$, as proposed in ref. 17. The region enclosed between the

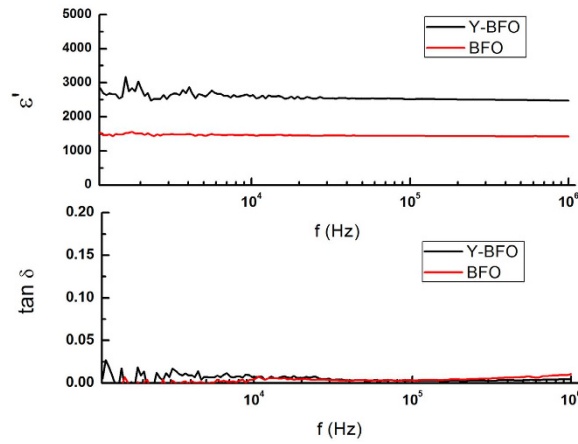


Figure 9. Dielectric constant and loss tangent values measured on Y-BFO and BFO samples for comparing purposes.

continuous lines, separating the main phases ferroelectric $R3c$ and paraelectric $O Pnma$, is the bridging mixed phase formed by nanometer-size antipolar domains in the $R3c$ matrix^{16,19}, which is thought to be responsible for the enhancement of the dielectric and electromechanical properties in these compositions. In order to transpose the diagram in terms of compositions, we have estimated the dependence of R_{av} on the dopant concentration x for the different RE ionic radii, including Y^{3+} . The corresponding ionic radii of the trivalent A ions in 12-fold coordination as given in refs 17,41,42 are: R_{Bi} (1.36 Å) > R_{Sm} (1.28 Å) > R_{Gd} (1.27 Å) > R_{Dy} (1.24 Å) > R_Y (1.22 Å). For every $Bi_{1-x}RE_xFeO_3$ composition the average ionic radius is plotted against x in Fig. 1(d). The horizontal lines mark the boundaries of the MPB region (near room temperature) as identified in Fig. 1(c). The square symbols on the Sm, Gd and Dy lines identify the compositions where the maxima of the dielectric and electromechanical responses have been obtained, as reported in ref. 17. The corresponding value of R_{av} is called critical ($R_{av,c}$) since it is common for all compositions, marking the transition from the $R3c$ to the $Pnma$ phase. Its significance is related to the difference in the free energy density between these two phases, $\Delta U(R_{av})$, which is given by the relationship¹⁷

$$\Delta U(R_{av}) = \Delta U_{BFO} - k(R_{av} - R_{Bi}) \quad (3)$$

where ΔU_{BFO} is the energy density difference for pure BFO and k is a constant. At the critical average ionic radius, $R_{av} = R_{av,c}$, $\Delta U(R_{av,c}) = 0$.

It can be observed that the corresponding compositions are placed within the limits of the MPB region. Moreover, Y-BFO films composition ($x = 0.05$), represented by the square point on the Y line and by the red square symbol in Fig. 1(c), is also inside the MPB region of the universal phase diagram. The smaller the ionic radius of the A-site RE dopant, the lower the concentration needed to induce the new phase. This is easy to understand if one recalls that the $O Pnma$ phase is favoured by tilt distortions of the oxygen octahedra which, at their turn, are promoted by small size ions occupying the A-site positions. It has been previously evidenced¹⁶⁻¹⁹ that such compositions show also the presence of nanodomains with different orientations which favor the enhancement of dielectric and piezoelectric response, by providing a low energy pathway for polarization rotation between different polar axes. As we have shown above, the presence of nanodomains is characteristic also for Y-BFO epitaxial films. Indeed, strain nanopatterns in geometric phase analysis are related to lattice distortions³², which in turn are associated in polar materials with local polarization variations³², therefore with nanodomains. One can use basically two approaches to correlate the dielectric permittivity ϵ to the peculiar nanodomain configuration. The first one is through the averaged polarization response to an electric field E :

$$\epsilon_{ij} = \frac{\partial \langle P_i \rangle}{\partial E_j} \quad (4)$$

where $\langle P_i \rangle$ is the domain-averaged polarization. Although a realistic model is difficult to construct, a simple case of a mixture of two stripe domain variants with different populations α and $1-\alpha$ has been considered in ref. 43 to obtain the following relation:

$$\epsilon_{ij} = P_s n_i \frac{\partial \alpha}{\partial E_j} \quad (5)$$

where P_s is domain saturation polarization and n_i is related to the polarization directions. It is evident from this equation that contributions arising from variations of populations of different nanodomains with electric field will greatly enhance the dielectric response. This has been indeed observed for different polar materials with nanodomain configurations^{44,45}.

The second approach is through the fluctuation-dissipation theorem⁴⁶, relating the dielectric permittivity to polarization fluctuations. Consider a ferroelectric with two coexisting phases with small energy difference. In this case the fluctuations of polarization occur mainly due to the libration (rotation) of the polarization vector⁴⁷ and they can be expressed as $\Delta\vec{P} = \vec{P} - \vec{P}_0$, where \vec{P}_0 is the easy polarization direction. These rotational fluctuations can be characterized by the thermodynamic average $\langle |\Delta\vec{P}_\perp|^2 \rangle$, where $\Delta\vec{P}_\perp$ is the projection of $\Delta\vec{P}$ on the plane which is normal to the easy polarization direction. In ref. 47, Khachatryan has shown that in the first approximation the thermodynamic average of polarization fluctuations can be written as

$$\langle |\Delta\vec{P}_\perp|^2 \rangle \propto \frac{kT}{\xi(\alpha - \alpha_c(\vec{P}_0, T))} \quad (6)$$

where ξ is a constant, α is the concentration of one of the coexisting phases and α_c is the critical concentration signaling the metastability limit, where the energy difference between the coexisting phases is minimum. It means that in the metastability region the domain wall energy γ , which is determined by this energy of polarization change within the domain boundary, becomes minimum and therefore nanodomains are formed, since the following relation

$$D \propto \sqrt{\gamma} \quad (7)$$

holds between γ and the domain size D . Furthermore, through the fluctuation-dissipation theorem, the dielectric permittivity is related to the averaged polarization fluctuations by the relationship

$$\varepsilon \propto \frac{1}{kT} \langle |\Delta\vec{P}_\perp|^2 \rangle \propto \frac{1}{\xi(\alpha - \alpha_c(\vec{P}_0, T))} \quad (8)$$

which means that the dielectric permittivity of the material diverges in the metastability limit.

We have seen that, in Y-BFO, the conditions for coexisting phases and nanodomain formations are created by Y-doping and epitaxial strain. We can infer therefore that the high dielectric permittivity of the $\text{Bi}_{0.95}\text{Y}_{0.05}\text{FeO}_3$ thin films is due to the nanoscale complex structure associated with the presence of competing phases at the MPB, promoted by both chemical pressure (Y-doping) and misfit strain caused by the epitaxial growth on the STO substrate.

Conclusions

We have obtained very high in-plane dielectric permittivity ($\varepsilon' \sim 2500$) and low dielectric loss ($\tan\delta < 0.01$) on Y-doped BiFeO_3 films epitaxially grown on $\text{SrTiO}_3(001)$ by pulsed laser deposition. Our experimental results reveal that the previously evidenced limitations on these values can be surmounted in high quality epitaxial films by promoting the formation of mixed states at nanoscale level. High resolution transmission electron microscopy and geometric phase analysis evidenced nanostripe domains with alternating compressive and tensile strain. Our work brings insight into the combined role of chemical pressure and epitaxial strain on the destabilization of ferroelectric phase and appearance of nanoscale stripe structure.

Methods

The films were grown by pulsed laser deposition on (001) SrTiO_3 (STO) single crystal substrates, from ceramic targets with composition $\text{Bi}_{0.95}\text{Y}_{0.05}\text{FeO}_3$ (Y-BFO) and BiFeO_3 (BFO). The thickness of the films was set around 100 nm, in order to preserve the strained condition. The deposition has been made under 13 Pa oxygen partial pressure, by using an ArF excimer laser (193 nm wavelength) with pulse frequency 5 Hz. The laser pulse energy was 20 mJ and the substrate temperature was 700 °C. In these conditions the growth rate was about 0.1 Å/s.

X-ray diffraction (XRD) at room temperature was performed with a PANalytical X'Pert MRD diffractometer, by using a line focused parallel monochromatic beam with $\text{CuK}\alpha 1$ radiation (0.1540598 nm) provided by a hybrid monochromator $2\text{xGe}(220)$ asymmetric.

The HR-TEM investigations have been performed on a JEM ARM 200F microscope.

Piezoforce microscopy (PFM) measurements have been carried out on a commercial AFM (XE-100, Park Systems) in order to evidence the local ferroelectric domain orientation.

For dielectric measurements two sets of Au interdigital electrodes with different dimensions have been deposited on top surfaces of the films by lift-off technique. Low-signal dielectric spectroscopy measurements have been carried out by using an HP4194A impedance bridge equipped with a special holder for contacting the IDE electrodes. In order to verify the correctness of the measurement method and of the calculation model, IDE structures have been deposited also directly on the STO substrate, and its dielectric constant has been measured and compared with datasheet value.

References

- Eerenstein, W., Mathur, N. D. & Scott, J. F. Multiferroic and magnetoelectric materials. *Nature* **442**, 759–765 (2006).
- Catalan, G. & Scott, J. F. Physics and Applications of Bismuth Ferrite. *Adv. Mater.* **21**, 2463–2485 (2009).
- Kubel, F. & Schmid, H. Structure of a ferroelectric and ferroelastic monodomain crystal of the perovskite BiFeO_3 . *Acta Cryst.* **B46**, 698–702 (1990).
- Fischer, P., Polomska, M., Sosnowska, I. & Szymanski, M. Temperature dependence of the crystal and magnetic structures of BiFeO_3 . *J. Phys. C.* **13**, 1931–1940 (1980).
- Kamba, S. *et al.* Infrared and terahertz studies of polar phonons and magnetodielectric effect in multiferroic BiFeO_3 ceramics. *Phys. Rev. B.* **75**, 024403 (2007).
- Guenou, M. *et al.* Multiple high-pressure phase transitions in BiFeO_3 . *Phys. Rev. B.* **84**, 174107 (2011).
- Yang, Y., Infante, Y. C., Dkhil, B. & Bellaiche, L. Strain effects on multiferroic BiFeO_3 films. *C. R. Physique.* **16**, 193 (2015).

8. Scarisoreanu, N. D. *et al.* High Permittivity $(1-x)\text{Ba}(\text{Zr}_{0.2}\text{Ti}_{0.8})\text{O}_3-x(\text{Ba}_{0.7}\text{Ca}_{0.3})\text{TiO}_3$ ($x=0.45$) Epitaxial Thin Films with Nanoscale Phase Fluctuations. *ACS Appl. Mater. Interfaces*. **7**, 23984–23992 (2015).
9. Xu, G. Y. *et al.* Low symmetry phase in (001) BiFeO₃ epitaxial constrained thin films. *Appl. Phys. Lett.* **86**, 182905 (2005).
10. Wang, H. W. *et al.* Strain-Induced Polarization Rotation in Epitaxial (001) BiFeO₃. *Phys. Rev. Lett.* **101**, 107602 (2008).
11. Kim, D. H., Lee, H. N., Biegalski, M. D. & Christen, H. M. Effect of epitaxial strain on ferroelectric polarization in multiferroic BiFeO₃ films. *Appl. Phys. Lett.* **92**, 012911 (2008).
12. Saito, K. *et al.* Structural Characterization of BiFeO₃ Thin Films by Reciprocal Space Mapping. *Jpn. J. Appl. Phys.* **45**, 7311–7314 (2006).
13. Kan, D. & Takeuchi, I. Effect of substrate orientation on lattice relaxation of epitaxial BiFeO₃ thin films. *J. Appl. Phys.* **108**, 014104 (2010).
14. Fu, H. & Cohen, R. E. Polarization rotation mechanism for ultrahigh electromechanical response in single-crystal piezoelectrics. *Nature* **403**, 281–283 (2000).
15. Fujino, S. *et al.* Combinatorial discovery of a lead-free morphotropic phase boundary in a thin-film piezoelectric perovskite. *Appl. Phys. Lett.* **92**, 202904 (2008).
16. Cheng, C. J., Borisevich, A. Y., Kan, D., Takeuchi, I. & Nagarajan, V. Nanoscale Structural and Chemical Properties of Antipolar Clusters in Sm-Doped BiFeO₃ Ferroelectric Epitaxial Thin Films. *Chem. Mater.* **22**, 2588–2596 (2010).
17. Kan, D. *et al.* Universal Behavior and Electric-Field-Induced Structural Transition in Rare-Earth-Substituted BiFeO₃. *Adv. Funct. Mater.* **20**, 1108–1115 (2010).
18. Yang, C.-H., Kan, D., Takeuchi, I., Nagarajan, V. & Seidel, J. Doping BiFeO₃: approaches and enhanced functionality. *Phys. Chem. Chem. Phys.* **14**, 15953–15962 (2012).
19. Cheng, C.-J. *et al.* Structural transitions and complex domain structures across a ferroelectric-to-antiferroelectric phase boundary in epitaxial Sm-doped BiFeO₃ thin films. *Phys. Rev. B*. **80**, 014109 (2009).
20. Sando, D., Barthelemy, A. & Bibes, M. BiFeO₃ epitaxial thin films and devices: past, present and future. *J. Phys.: Condens. Matter*. **26**, 473201 (2014).
21. Liu, H., Yang, P., Yao, K. & Wang, J. Growth rate induced monoclinic to tetragonal phase transition in epitaxial BiFeO₃ (001) thin films. *Appl. Phys. Lett.* **98**, 102902 (2011).
22. Liu, H. *et al.* Origin of a Tetragonal BiFeO₃ Phase with a Giant c/a Ratio on SrTiO₃ Substrates. *Adv. Funct. Mater.* **22**, 937–942 (2012).
23. Ren, P. *et al.* Temperature controlled c axis elongated low symmetry phase BiFeO₃ thin film on STO substrate. *AIP Adv.* **3**, 012110 (2013).
24. Glazer, A. M. Simple ways of determining perovskite structures. *Acta Cryst.* **A31**, 756–762 (1975).
25. Wu, Y.-J. *et al.* Pressure effect on structural and vibrational properties of Y-substituted BiFeO₃. *J. Phys. Condens. Matter*. **25**, 365401 (2013).
26. Christen, H. M., Nam, J. H., Kim, H. S., Hatt, A. J. & Spaldin, N. A., Stress-induced $R-MA-MC-T$ symmetry changes in BiFeO₃ films. *Phys. Rev. B* **83**, 144107 (2011).
27. Wang, J. *et al.* Epitaxial BiFeO₃ Multiferroic Thin Film Heterostructures. *Science* **299**, 1719–1722 (2003).
28. Chu, Y. H. *et al.* Ferroelectric size effects in multiferroic BiFeO₃ thin films. *Appl. Phys. Lett.* **90**, 252906 (2007).
29. Williamson, G. K. & Hall, W. H. X-ray line broadening from filed aluminium and wolfram. *Acta Metall.* **1**, 22–31 (1953).
30. Chierchia, R. *et al.* Microstructure of heteroepitaxial GaN revealed by x-ray diffraction. *J. Appl. Phys.* **93**, 8918–8925 (2003).
31. Metzger, T. *et al.* Defect structure of epitaxial GaN films determined by transmission electron microscopy and triple-axis X-ray diffractometry. *Philos. Mag. A* **77**, 1013–1025 (1998).
32. Hÿtch, M. J., Snoeck, E. & Kilaas, R. Quantitative measurement of displacement and strain fields from HREM micrographs - Electron Diffraction Effects due to Modulated Structures. *Ultramicroscopy* **74**, 131–146 (1998).
33. Liu, H. *et al.* Thickness-dependent twinning evolution and ferroelectric behavior of epitaxial BiFeO₃ (001) thin films. *Phys. Rev. B*. **82**, 064108 (2010).
34. Martin, L. W. & Ramesh, R., Multiferroic and magnetoelectric heterostructures. *Acta Mater.* **60**, 2449–2470 (2012).
35. Farnell, G. W., Cermak, I. A., Silvester, P. & Wong, S. K. Capacitance and field distributions for interdigital surface-wave transducers. *IEEE Trans. on Sonics and Ultrasonics* **SU-17**, 188–195 (1970).
36. Al-Shareef, H. N., Dimos, D., Raymond, M. V., Schwartz, R. W. & Mueller, C. H. Tunability and calculation of the dielectric constant of capacitor structures with interdigital electrodes. *J. Electroceram.* **1**(2), 145–153 (1997).
37. Feigl, L. *et al.* Controlled stripes of ultrafine ferroelectric domains. *Nat. Commun.* **5**, 4677 (2014).
38. Yao, J., Yang, Y., Ge, W., Li, J. & Viehland, D. Domain Evolution in $\text{PbMg}_{1/3}\text{Nb}_{2/3}\text{O}_3$ -60at% PbTiO_3 with Temperature and Electric Field. *J. Am. Ceram. Soc.* **94**, 2479–2482 (2011).
39. Nelson, C. T. *et al.* Spontaneous Vortex Nanodomain Arrays at Ferroelectric Heterointerfaces. *Nano Lett.* **11**, 828–834 (2011).
40. Qi, Y. *et al.* Temperature-driven evolution of hierarchical nanodomain structure in tetragonal-like BiFeO₃ films. *Appl. Phys. Lett.* **100**, 022908 (2012).
41. Shannon, R. D. Revised effective ionic radii and systematic studies of interatomic distances in halides and chalcogenides. *Acta Crystallogr. A*. **32**, 751–767 (1976).
42. Jia, Y. Q. Crystal radii and effective ionic radii of the rare earth ions. *J. Solid State Chem.* **95**, 184–187 (1991).
43. Rossetti, Jr., G. A., Khachatryan, A. G., Akcay, G. & Ni, Y. Ferroelectric solid solutions with morphotropic boundaries: Vanishing polarization anisotropy, adaptive, polar glass, and two-phase states. *J. Appl. Phys.* **103**, 114113 (2008).
44. Schönau, K. A. *et al.* Nanodomain structure of $\text{Pb}[\text{Zr}_{1-x}\text{Ti}_x]\text{O}_3$ at its morphotropic phase boundary: Investigations from local to average structures. *Phys. Rev. B* **75**, 184117 (2007).
45. Theissmann, R. *et al.* Nanodomains in morphotropic lead zirconate titanate ceramics: On the origin of the strong piezoelectric effect. *J. Appl. Phys.* **102**, 024111 (2007).
46. Lines, M. E. & Glass, A. M. *Principles and Applications of Ferroelectrics and Related Materials* (Clarendon Press, 1977).
47. Khachatryan, A. G. Ferroelectric solid solutions with morphotropic boundary: Rotational instability of polarization, metastable coexistence of phases and nanodomain adaptive states. *Philos. Mag.* **90**, 37–60 (2010).

Acknowledgements

The authors M. Dinescu and N. D. Scarisoreanu gratefully acknowledge the financial support from RSRP 18 RO-CH and IZERZO-142176/1 projects. V. Ion thanks the financial support POSDRU/159/1.5/S/137750 project. V. Teodorescu, C. Ghica and R. Negrea acknowledge UEFISCDI for the financial support within the PN-II-ID-PCE-2011-3-0268 project.

Author Contributions

N.D.S. and M.D. conceived and designed the experiments. F.C. performed dielectric measurements. V.I. and R.B. conducted XRD and PFM analysis. C.G., R.N. and V.S.T. conducted HR-TEM and GPA analysis on the samples. F.C., N.D.S., R.B. and M.D. co-wrote the paper. All authors discussed and reviewed the manuscript.

Additional Information

Supplementary information accompanies this paper at <http://www.nature.com/srep>

Competing financial interests: The authors declare no competing financial interests.

How to cite this article: Scarisoreanu, N. D. *et al.* Joining Chemical Pressure and Epitaxial Strain to Yield Y-doped BiFeO₃ Thin Films with High Dielectric Response. *Sci. Rep.* **6**, 25535; doi: 10.1038/srep25535 (2016).



This work is licensed under a Creative Commons Attribution 4.0 International License. The images or other third party material in this article are included in the article's Creative Commons license, unless indicated otherwise in the credit line; if the material is not included under the Creative Commons license, users will need to obtain permission from the license holder to reproduce the material. To view a copy of this license, visit <http://creativecommons.org/licenses/by/4.0/>